Geomechanics and Engineering, *Vol. 7, No. 6 (2014) 613-631*
DOI: http://dx.doi.org/10.12989/gae.2014.7.6.613

Computational modeling of buried blast-induced ground motion and ground subsidence

Zhi-Chao Zhang [1], Han-Long Liu [1], Ronald Y.S. Pak *[2] and Yu-Min Chen [1]

[1] *College of Civil and Transportation Engineering, Hohai University, Nanjing, China*
[2] *Department of Civil, Environmental & Architectural Engineering, University of Colorado, Boulder, CO, USA*

(*Received March 12, 2014, Revised August 13, 2014, Accepted August 14, 2014*)

Abstract. To complement the method of field-scale seismic ground motion simulations by buried blast techniques, the application and evaluation of the capability of a numerical modeling platform to simulate buried explosion-induced ground motion at a real soil site is presented in this paper. Upon a layout of the experimental setup at a level site wherein multiple charges that were buried over a large-diameter circle and detonated in a planned sequence, the formulation of a numerical model of the soil and the explosives using the finite element code LS-DYNA is developed for the evaluation of the resulting ground motion and surface subsidence. With a compact elastoplastic cap model calibrated for the loess soils on the basis of the site and laboratory test program, numerical solutions are obtained by explicit time integration for various dynamic aspects and their relation with the field blast experiment. Quantitative comparison of the computed ground acceleration time histories at different locations and induced spatial subsidence on the surface afterwards is given for further engineering insights in regard to the capabilities and limitations of both the numerical and experimental approaches.

Keywords: buried explosion; field tests; numerical method; earthquakes; ground motion; ground subsidence

1. Introduction

The dynamic response of a site in earthquakes has always been a major research challenge in geotechnical engineering and soil dynamics. At the elemental level, much of past experimental research has been done using laboratory cyclic triaxial, simple shear and resonant column tests (e.g., Rutherford and Biscontin 2013, Ashlock *et al*. 2013, Nair and Latha 2012, Vaid and Sivathayalan 1996, Bates 1989). Earthquake effects on soil structures or foundations have also been studied as physical boundary value problems by mean of shake table and centrifuge modeling methods (e.g., Pak *et al*. 2011, Elgamal *et al*. 2005, Wang *et al*. 2011b, Gao *et al*. 2011). While these approaches can provide valuable information on the basic behavior of soils, they often cannot reproduce details of actual field conditions such as the in-situ stress state, cementation, past stress story, ground water, local layering (e.g., Dou and Byrne 1997, Garga 1988, Santagata and Germaine 2005). Because of their cost and complexity, field scale experimental results remain limited in soil dynamics and earthquake engineering. Owing to the unpredictability of earthquakes,

---

*Corresponding author, Professor, E-mail: pak@colorado.edu

http://www.techno-press.org/?journal=gae&subpage=7 ISSN: 2005-307X (Print), 2092-6219 (Online)

an instrumented site may take years before an earthquake will occur. Moreover, real earthquakes are one-time events and do not provide the opportunity for parametric studies which are keys to a thorough understanding of the problem. Powerful enough to generate significant ground motion in full-scale situations, buried explosive blasts have been employed to generate data relevant to seismic engineering research (e.g., Al-Qasimi *et al.* 2005, Wang *et al.* 2011a, Ashford and Rollins 2004, Wang *et al.* 2002). As in all experimental simulations, however, direct interpretation of the results can be tenuous as the number of tests and sensors are limited and the site condition cannot be varied easily.

To obtain the maximum benefits from such seismic field blast testing, a companion computational geomechanics platform can be extremely useful (e.g., Kim 2009, Mamalis *et al.* 2011). With pertinent parametric calibrations of the numerical model, it can assist the choice of charge weights and spatial layout for further field testing as well as provide a rational basis to evaluate or even predict field performance of structures and foundation under similar site and seismological conditions. In this paper, the application and evaluation of the capability of a numerical modeling platform to simulate buried explosion-induced ground motion at a real soil site is presented. Founded on explicit time integration methods, the finite element code LS-DYNA (Hallquist 2012) is employed to evaluate the ground motion and surface subsidence generated in a field-scale buried-blast experimental program (Wang *et al.* 2011a) in which multiple explosive charges are buried around a large-diameter circle and detonated in a planned sequence. With a continuum elastoplastic cap model for the soil, the computed acceleration time histories and seismic subsidence are compared to the in-situ field measurements of accelerations and final surface settlements. Insights on the calibration and capabilities of the numerical method for blast-generated ground motions are highlighted.

2. Earthquake field simulation by buried explosive blasts

2.1 Experimental test site at Gansu, China

The test site is located in the fourth terrace of the Yellow River valley, the south field of Lijiawan Ping near Lijiawan village of Gansu province (Wang *et al.* 2011a). Data obtained by two exploratory wells over depth show that there are four soil layers overlaying a Tertiary red bed. At the top, it is a thin arable layer, followed by two layers of different loess and then a pebble bed. The first layer of loess, the seismic subsidence loess (Wang *et al.* 2011a), has a thickness of 14 m. It has a typical physical characteristic of collapsible loess, with a loose soil mass and large void

Table 1 Physical properties of the loess layer (Wang *et al.* 2011a)

Soil	Depth of sample (m)	Density (g/cm^3)		Water content (%)	Void ratio
		Nature	Dry		
Seismic subsidence loess	4	1.47	1.32	12.5	1.045
	8	1.48	1.29	15.2	1.101
	12	1.49	1.28	14.8	1.109
Secondary loess	16	1.48	1.33	10.3	1.026
	20	1.54	1.42	8.4	0.911

Table 2 Shear strength of loess with different water ratio (Li *et al*. 2007)

Sample	ρ_d (g/cm^3)	Water content (%)	c (kPa)	φ (°)
undisturbed	1.26	5	78.45	33.6
		12	59.31	24.3
		17.8	39.02	22.4
		26	30.69	21.2
		42.5 (saturated)	18.19	18.4

Table 3 Strength parameters c and φ of different loess layers

Depth (m) parameter	0-8	8-16	16-24	24-28
Water content (%)	12.5	14.8	8.4	8.4
frictional angle (φ, degree)	24	23.4	28.2	28.2
Cohesion (c, kPa)	58	50	69	69

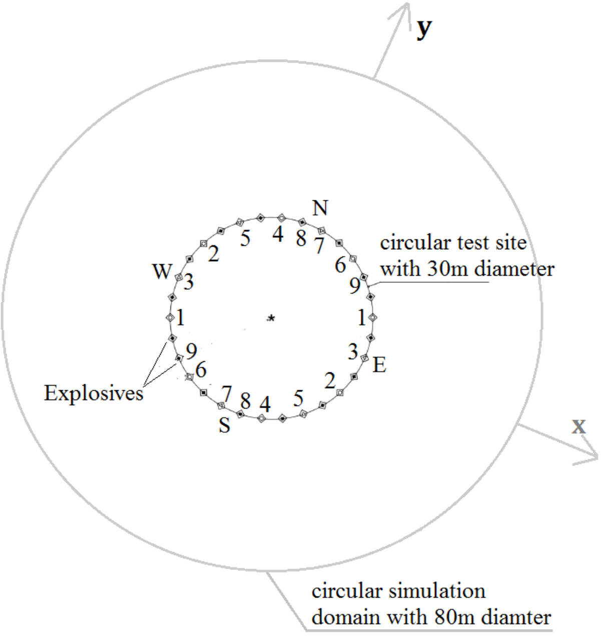

Fig. 1 Layout of explosives in the field blast testing (Wang *et al*. 2011a)

ratio. In this loess layer, water content of soil varies from 12% to 16%, and clay particles are visible at some positions. The characteristics of the secondary loess in the lower layer with a thickness of 13 m has a water content of less than 10% and a higher clay content.

The key physical properties of the loess layer at the depth of 4, 12, 16 and 20 m are listed in Table 1 (Wang *et al*. 2011a). Based on laboratory soil testing and correlation such as the one in Table 2 for the loess (Li *et al*. 2007), representative strength parameters and water content of the soil in 0-8 m, 8-16 m, 16-24 m, 24-28 m are given in Table 3.

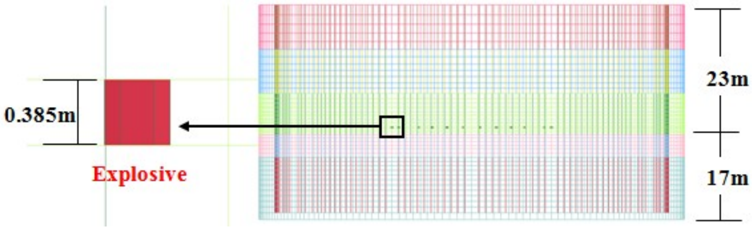

Fig. 2 Enlargement of the explosive elements

2.2 Instrumentations in the blasting test

The layout of explosives in the field blast testing is shown in Fig. 1 (Wang *et al*. 2011a). Thirty explosive charges, each of which is 40 kg No. 2 rock explosive (Liu *et al*. 2004), were buried in a circular configuration with a radius of 30 m and at a depth of 23 m. They consisted of 15 diametrically opposite pairs of explosive charges. They were detonated with a measured time between 655-760 ms with 9 pairs of them successful. The actual blast sequence is indicated in Fig. 1 where the order and location of the firing pairs are indicated, and the explosives without numbers are those that failed to detonate in the field test. Thirty-seven observation points within the ring of explosives and 43 observation points outside the ring of explosives were used to measure the seismic subsidence of the soil after the blast event. There were 24 accelerometers to capture the motion time histories of the ground surface during blasting. The farthest accelerometer is located at the position with a 110 m distance from the center of the test site and along the azimuthal angle of 33.3°. More details can be found in reference Wang *et al*. (2011a).

3. Finite element modeling of blast tests

3.1 Spatial domain of model

Based on the layout of the field test, a cylindrical soil domain with a diameter of 80 m and a height of 40 m is modeled numerically (Figs. 2-3) with the *x*-, *y*- and *z*-axes representing the East-West, North-South and depthwise directions respectively. The loess in the finite element domain is divided into 4 layers at the depth of 0-8 m, 8-16 m, 16-24 m and 24-28 m, and the depth of 28 below belongs to gravel and red rock layer. To allow wave radiation to the far field while providing the lateral support for the soil medium, a viscoelastic thin layer (Hallquist 2012) is used at the circumferential boundary of the finite element model.

3.1.1 Finite element mesh

All the elements in the finite element mesh are 8-node hexahedral elements. A finer 3D mesh is used near the explosives where the response's magnitude and gradient will be high. In total, 417,690 hexahedral elements and 424,032 nodes were used, with element aspect ratios generally smaller than 1:4 and their size's variation gradual.

3.1.2 Boundary conditions

The model was initialized to account for gravitational loading on the soil mass over a 2-second

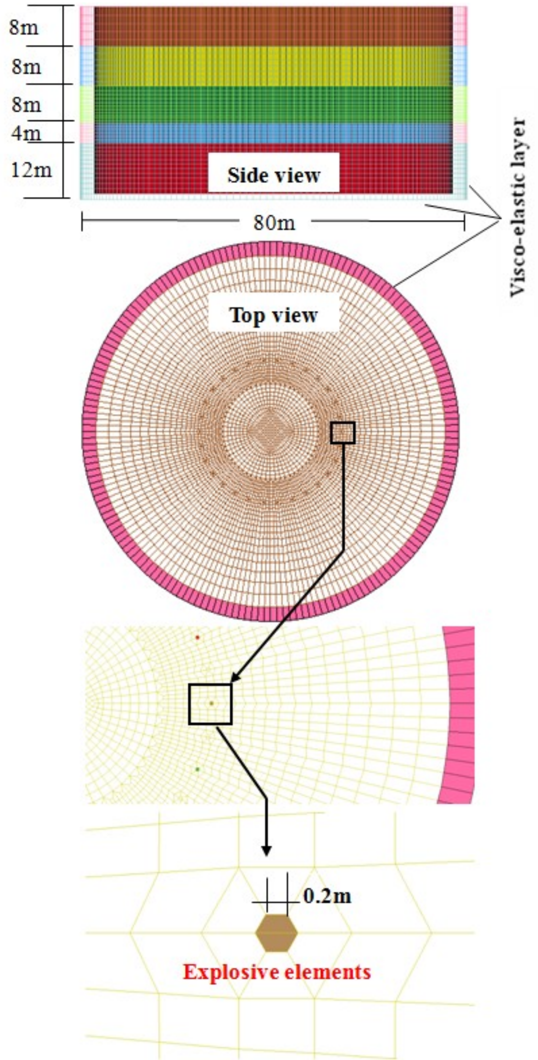

Fig. 3 FEM model and its enlargement

period. Roller boundaries were applied to the bottom and circumference during this set-up phase. When the proper stress state was established, the outer boundary of the absorbing layer and the bottom were changed to the zero-displacement condition for the explosion phase of the simulation.

3.1.3 Delay time of explosion and simulation time

Owing to the fast rise-time in the explosive event, the time step used in the explicit time integration is of the order of microseconds. The 9 pairs of sequential buried explosions in the field test were simulated by LS-DYNA for a time period of 10 sec, taking into account of the time sequencing of detonations as noted in Table 4 and (Wang *et al*. 2011a).

3.2 Physical model

Table 4 Blasting sequence in the numerical simulation

Blasting sequence	T_1	T_2	T_3	T_4	T_5	T_6	T_7	T_8	T_9
Detonation time/s	2	2.76	3.42	4.10	4.80	5.40	6	6.5	7.15

3.2.1 Constitutive modeling of loess

A key to the numerical simulation of the soil ground motion is the constitutive model for the soil. In this study, the compact elastoplastic Geologic Cap model (DiMaggio and Sandler 1971, Hallquist 2012) in LS-DYNA is adopted**.** The plastic yield surface in this model consists of three regions (Fig. 4): a shear failure envelope $f_1(\sigma)$, an elliptical cap $f_2(\sigma, \kappa)$, and a tension cutoff region $f_3(\sigma)$, where σ is the stress tensor and κ is a hardening parameter. The functional forms of the three surfaces are:

(a) For shear failure region where $T \le I_1 < L(\kappa)$

$$f_1(\sigma) = \sqrt{J_2} - F_e(I_1) = 0 \tag{1}$$

(b) For elliptical cap region where $L(\kappa) \le I_1 < X(\kappa)$

$$f_2(\sigma, \kappa) = \sqrt{J_2} - F_c(I_1, \kappa) = 0 \tag{2}$$

(c) For tension cutoff region where $I_1 \equiv T$

$$f_3(\sigma) = T - I_1 = 0 \tag{3}$$

where I_1 is the first invariant of the stress tensor and J_2 is the second invariant of the deviator stress tensor, T is the tension cutoff value. In Eq. (1), $F_e(I_1)$ is expressed as

$$F_e(I_1) = \alpha - \gamma e^{-\beta I_1} + \theta I_1 \tag{4}$$

with γ and β set to zero in this study so that α *and* θ can be directly related to the classical Mohr-Coulomb parameters c and φ. In Eq. (2), $F_c(I_1, \kappa)$ is expressed as

$$F_c(I_1, \kappa) = \frac{1}{R}\sqrt{[X(\kappa) - L(\kappa)]^2 - [I_1 - L(\kappa)]^2} \tag{5}$$

$$X(\kappa) = \kappa + RF_e(\kappa) \tag{6}$$

$$L(\kappa) = \begin{cases} \kappa & \text{if} \quad \kappa > 0 \\ 0 & \text{if} \quad \kappa \le 0 \end{cases} \tag{7}$$

where R is the shape factor and the ratio of major to minor axes of the elliptical cap. $X(\kappa)$ is the intersection of the cap surface with the I_1 axis and the hardening parameter κ is related to the plastic volume change ε_v^p through the hardening law

$$\varepsilon_v{}^p = W\left\{1 - e^{-D[X(\kappa) - X_0]}\right\} \tag{8}$$

in which the values of parameters W and D can be obtained from hydrostatic compression test data. Note that W characterizes the ultimate plastic volumetric strain, D denotes the total volumetric plastic strain rate, and X_0 determines the initiation of volumetric plastic deformation under hydrostatic loading conditions.

(a) Cap model strength parameters

With γ and β set to zero as noted earlier, the shear failure surface is defined by

$$f_1(\sigma) = \sqrt{J_2} - (\alpha + \theta I_1) = 0 \tag{9}$$

in terms of α and θ. Adopting the common approach of matching the shear strength given by Eq. (9) to Mohr-Coulomb's compressive meridian, α and θ are expressible in terms of c and φ (Chen and Saleeb 1994) through

$$\alpha = \frac{6 \cdot c \cdot \cos\phi}{\sqrt{3} \cdot (3 - \sin\phi)} \tag{10}$$

$$\theta = \frac{2 \cdot \sin\phi}{\sqrt{3} \cdot (3 - \sin\phi)} \tag{11}$$

and the conventional shear strength parameters given in Table 3 can be translated to the geologic cap parameters in Table 5.

(b) Cap surface parameter X_0

The parameter X_0 represents the intersection of the initial cap surface with the I_1-axis in the stress space and defines the size of the initial elastic domain of the soil. It can be determined from hydrostatic compression test data, i.e., pressure-volume response, when the pressure-volume response transitions from elastic to elastic-plastic. As the initial elastic domain of the soil is expected to increase with depth in relation to the in situ stress state, $X_0/3$ is estimated to be close to the mean stress σ_{mean}. Starting with $X_0 = 3^*\sigma_{\text{mean}}$, the final choice of X_0 for each layer is listed in Table 6.

(c) Elastic soil modulus

With reference to the experimental results in Luo (2000) on the modulus of loess with low degree of saturation, the reference shear modulus G was calculated according to

Table 5 Translation of Mohr-Coulomb shear strength parameters c and φ into cap model parameters α and θ

Depth (m) parameter	0-8	8-16	16-24	24-28
Water content (%)	12.5	14.8	8.4	8.4
Frictional angle (φ, degree)	24	23.4	28.2	28.2
Cohesion (c, kPa)	58	50	69	69
α (kPa)	70	61	83	83
θ	0.18	0.176	0.21	0.21

$$G = A_g K_c{}^{0.75} \frac{(2.973 - e_0)^3}{1 + e_0} (\sigma_{mean})^{\frac{1}{2}} \tag{12}$$

and the corresponding bulk modulus K as (Fung and Tong 2001)

$$K = \frac{2G(1+\nu)}{3(1-2\nu)} \tag{13}$$

In the above, σ_{mean} is in kPa, ν is the Poisson's ratio which is taken to be 0.35 for the loess as noted in Luo (2000), e_0 is the void ratio, K_c is the ratio of vertical to lateral stress estimated by $(1-\nu)/\nu = 1.857$ for the normally consolidated soil condition, and A_g is a material constant. For the loess at the site, the soil constant A_g is found to be $745(\text{kPa})^{0.5}$ (see Luo 2000). With the material parameters as chosen, Eqs. (12)-(13) are reduced to

$$G = 1185 \frac{(2.973 - e_0)^3}{1 + e_0} (\sigma_{mean})^{\frac{1}{2}} \tag{14}$$

$$K = \frac{2G(1+\nu)}{3(1-2\nu)} = 3G \tag{15}$$

A summary of the values of X_0, shear modulus G and bulk modulus K of soils at the depth of 4 m, 12 m, 20 m and 26 m can be found in Table 6 and the yield surfaces of different layers are illustrated in Fig. 4.

3.2.2 Constitutive modeling of gravel and red rock

For the gravel-red rock layer between the depth of 28-40 m, the linear elastic constitutive

Table 6 Parameters of cap model at different soil layers

Depth (m) parameter	0-8	8-16	16-24	24-28
e_0 (Void ratio)	1.045	1.109	0.911	0.911
Density (kg/m^3)	1470	1490	1540	1540
σ_{mean} (kPa)	40	121	203	267
X_0 (kPa)	96	290	487	640
G (MPa)	26	40	77	89
K (MPa)	78	120	231	267
α (kPa)	70	61	83	83
θ (radian)	0.18	0.176	0.21	0.21
β (MPa^{-1})	0	0	0	0
γ (MPa)	0	0	0	0
W	2.5	2.5	2.5	2.5
D (MPa^{-1})	7.25e-3	7.25e-3	7.25e-3	7.25e-3
R	1	1	1	1
Tension cutoff (kPa)	-100	-100	-100	-100

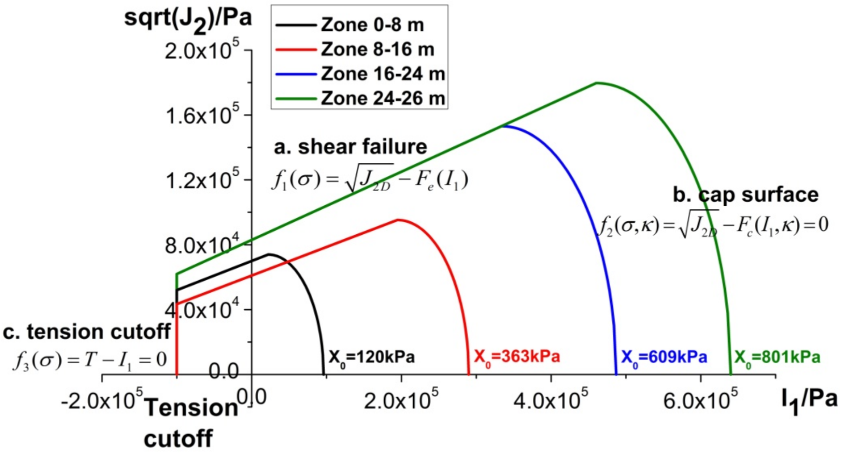

Fig. 4 Initial yield surfaces of different loess layers

Table 7 Parameters of pebble layer at the depth of 28-40 m

Parameters	Density (kg/m^3)	Young’s modulus (MPa)	Poisson’s ratio
Value	2000	1000	0.33

Table 8 Parameters of viscoelastic layers at different depths

Depth (m) parameter	0-8	8-16	16-24	24-28	28-40
Density	1470	1490	1540	1540	2000
K (MPa)	78	120	231	267	1000
G_0 (MPa)	36	50	87	99	386
G_∞ (MPa)	16	30	67	79	366
λ (s^{-1})	1	1	1	1	1

model is deemed appropriate for the loading considered. The elastic parameters are listed in Table 7.

3.2.3 Constitutive modeling of viscoelastic thin layer

In order to provide the lateral support for the soil medium in establishing the initial gravitational stress while allowing the transmission of waves from interior sources, a thin viscoelastic layer is placed at the outer lateral and bottom boundary of the soil domain with the same mechanical properties as the surrounding soil element in the corresponding depth.

The shear relaxation behavior (Hallquist 2012) of the viscoelastic layers is taken to be

$$G(t)=G_\infty+(G_0-G_\infty)e^{-\lambda t} \tag{16}$$

where K is the bulk modulus, G_∞ is long-time (infinite) shear modulus, G_0 is short-time shear modulus, and λ is the decay constant that can best minimize the wave reflection. The parameters of the viscoelastic layers employed are shown in Table 8.

Table 9 Parameters of No. 2 rock explosive charges

Parameter	A (GPa)	B (GPa)	R_1	R_2	ρ (kg/m^3)	E (GP)	ω	D (m/s^2)
Value	214	0.182	4.15	0.95	1000	4.5	0.30	3600

3.2.4 Equation of State for explosive charges

To describe the detonation of the No. 2 rock explosive charge in the numerical simulation, Jones-Wilkens-Lee (JWL) equation of state (Hallquist 2012) is employed to model the pressure generated from the expansion of the detonation product of the chemical explosive. The relationship of JWL can be written as

$$P_{eos} = A\left(1-\frac{\omega}{R_1 V}\right)e^{-R_1 V} + B\left(1-\frac{\omega}{R_2 V}\right)e^{-R_2 V} + \frac{\omega E}{V} \tag{17}$$

where P_{eos} is the pressure, V is a dimensionless relative specific volume, E is the internal energy density per unit volume, and the values of constants A, B, R_1, R_2, and ω have been determined from explosion experiments before. To account for the effect of combustion on detonation dynamics, at any time, the blast pressure $p$in an explosive element is given by (Hallquist 2012)

$$p = P_{eos} \times \max(F_1, F_2) \tag{18}$$

where the burn fractions F_1 and F_2 are

$$F_1 = \begin{cases} \dfrac{2(t-t_1)DA_{e\max}}{3v_e} & if\ t > t_1 \\ 0 & if\ t \le t_1 \end{cases} \tag{19}$$

$$F_2 = \frac{1-V}{1-V_{CJ}} \tag{20}$$

where V_{CJ} is the Chapman-Jouguet relative volume, t is current time, t_1 is the lighting time computed for each finite element by dividing the distance from the detonation point to the center of the explosive element by the detonation velocity D, A_{emax} is the maximum cross sectional area and v_e is the volume of explosive element. The calibrated parameters in Eqs. (17)-(20) for No. 2 rock explosive charges (Liu *et al.* 2004) are listed in Table 9.

4. Numerical results and comparison

The first phase of loading in the simulation is gravity loading. It is imposed as a body force field gradually with modest mass proportional damping as indicated in Fig. 5. The resulting vertical stress distribution at the end of the loading is uniform horizontally as expected (see Fig. 6).

4.1 Blast wave propagation due to explosions

As an initial check of the numerical model for the experimental blast sequence, the simulated

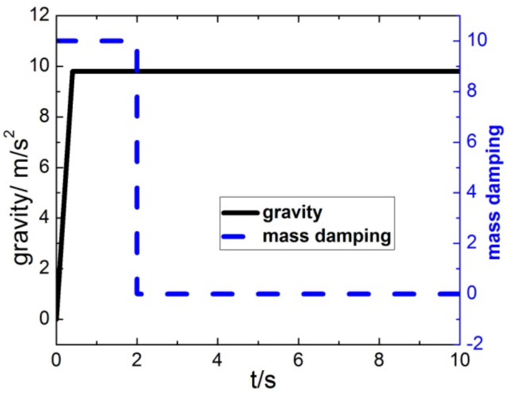

Fig. 5 Gravitational loading and mass damping of the model

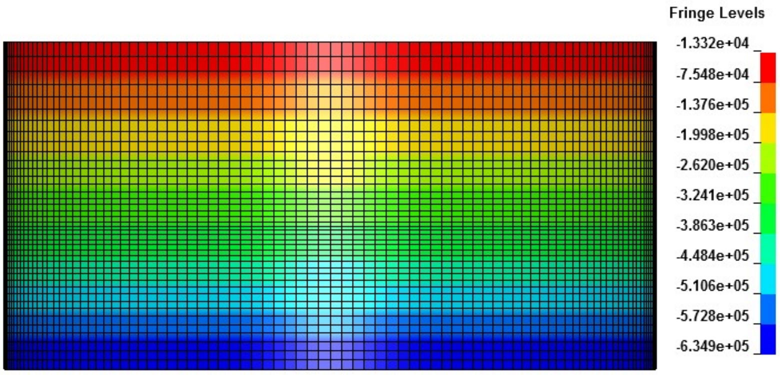

Fig. 6 Initial vertical stress distribution under gravity

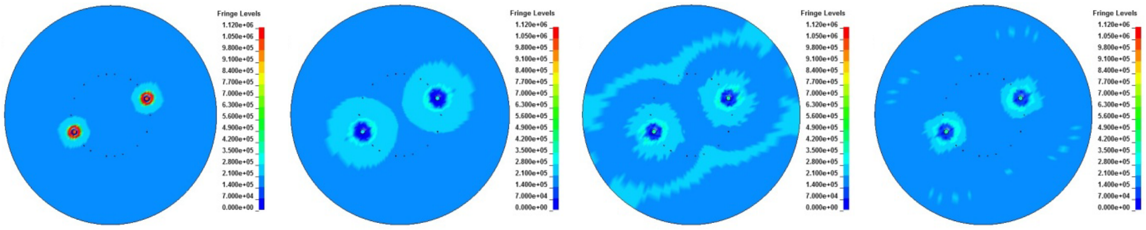

(a) $t = 2.01$ s (b) $t = 2.03$ (c) $t = 2.07$ (d) $t = 2.10$ s

Fig. 7 Blast pressure nephogram of first pair of explosives (detonated at time = 2 sec)

mean soil pressure response caused by the blast waves generated by the sequential detonation of two adjacent pairs of diametrically opposite explosive charges is first examined. The blast pressure nephograms after the first and second pairs of explosive charges at the depth of 23 m are shown in Figs. 7-8, respectively. As expected, the surface disturbance travels radially outward with rapidly decreasing amplitude. One can see that the two strands of blast waves are propagating at about the same speed from the symmetric detonation in the ideal finite element analysis. When the blast

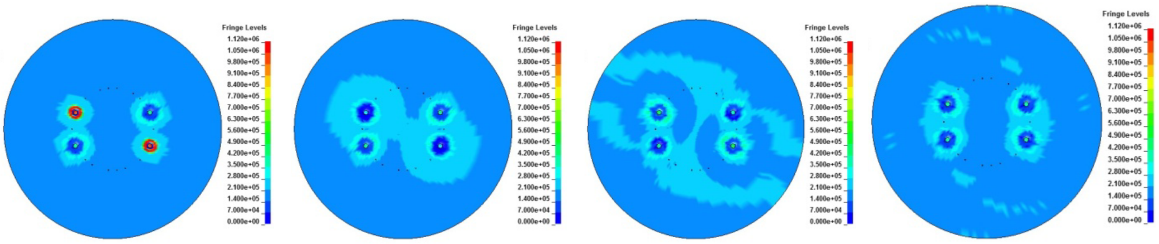

(a) $t = 2.77$ s (b) $t = 2.79$ s (c) $t = 2.82$ s (d) $t = 2.86$

Fig. 8 Blast pressure nephogram of second pair of explosives (detonated at time = 2.76 sec)

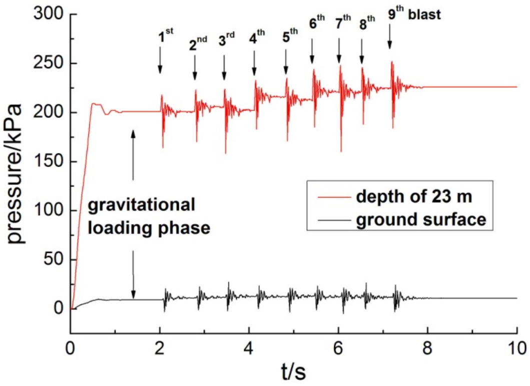

Fig. 9 Simulated pressure time histories at ground surface and at depth of 23 m in the middle of test site

waves reach the outer boundary of the model, minimal reflections can be seen in Figs. 7(c) and 8(c) with the aid of the viscoelastic lateral boundary.

At about 0.1 sec after the 1st and 2nd pairs of detonations respectively, that is at the time of T_1 + 0.1 s (Fig. 7(d)) and T_2 + 0.1 s (Fig. 8(d)), respectively, one can see that in most area of the test site, the high intensity blast pressure waves induced by each pair of detonations have subsided significantly before the onset of the next pair because of the delay in detonation times. During the successive explosion sequence, waves created by the two adjacent pairs of explosive charges also arrive at the center of test site at about the same time.

Proceeding to the simulation of the full sequential detonation of the 9 pairs of buried explosives with the actual time delays shown in Table 4, a plot of the computed blast pressure time history for an element in the center of the test site at the burial depth of 23 m (the plane where charges were laid) and one at the ground surface is shown in Fig. 9. Note that the distance from the element at the burial depth of 23 m to the explosion source is 15 m, while the distance from the element on the ground surface to the explosion source is about 27.46 m.

As indicated in the Fig. 9, there are 9 sharp pulses in the pressure-time plot for the element at the depth of 23 m, correlating well with the 9 sequential detonations. The pressure begins to change significantly at about 2.025 sec, after the first detonation which occurred at 2 sec. This indicates that the blast-induced compression wave traveled 15 m from the blast center with an average wave velocity of about 600 m/sec, correlating well with the field measured compression wave (P-wave) velocity of about 450-700 m/s (Wang *et al.* 2011a).

For the soil element located on the ground surface which is also farther away from the explosion source, the pressure level is much lower with a time history that exhibits a similar sequence of pulses but of smaller amplitudes. Due to the interaction of the incident blast wave and its reflection from the ground surface, the soil pressure on the ground surface exhibits a pattern with positive and negative pressure in turns. This is also the reason for the potential “stripping” and “throwing” of the soil near the ground surface as well as crater formation even when the burial depth of the explosive charges is relatively deep (Henrych 1979).

Compared to their initial in-situ stress levels, the mean stress in both elements increased after the blasting sequence. This residual increase in mean stress from the compression wave-dominant explosion-simulated ground motion is not commonly seen in shear wave-dominant natural

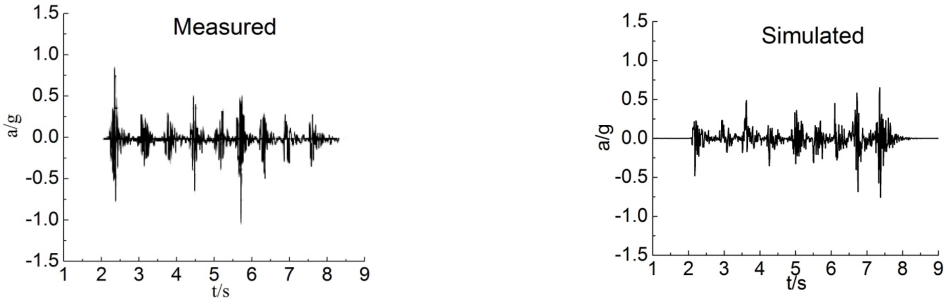

(a) Measured and simulated *x*-acceleration time histories

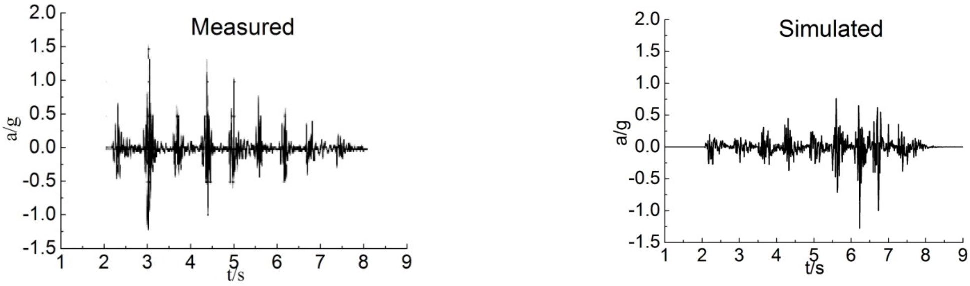

(b) Measured and simulated *y*-acceleration time histories

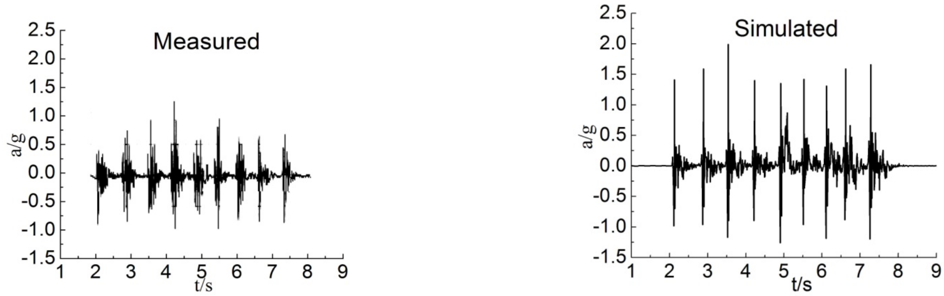

(c) Measured and simulated *z*-acceleration time histories

Fig. 10 Comparison of measured and simulated acceleration time histories at ground surface in the center of test site earthquake wave and should be noted by experimental planners. As expected, the closer the soil is to the explosion source, the more intense the pressure increase is found.

Moving on to the ground motion produced on the ground surface,the accelerations of the *x*-, *y*- and *z*-components from the finite element model are corresponding to the east-west (EW), north-south (NS) and depthwise (UD) directions of the test site, respectively. The comparison of the measured and simulated acceleration is shown Fig. 10. In the plots, each measured acceleration time history exhibits 9 clear spikes corresponding to the strong ground motion generated by the 9 pairs of explosive detonations. One can see that the simulated and measured acceleration time histories for the *x*- and *y*-directions are reasonably close, with the field measurements being slightly larger in the peak amplitude. The opposite however is true for vertical acceleration. This can be a result of the damping aspect as well as taking the underlying half-space of pebble and soft rock as being rigid which can lead to stronger compressional wave reflections. What is more, the discrepancy may also be due to that the real loess is cross-anisotropic while the constitutive model used in the simulation is isotropic.

In addition to the measurements at the center of the test site, 3 acceleration measurements at 20 m, 25 m and 30 m away north of the center of the test site were also used in the comparison to gain some insights about the spatial attenuation of the generated motion. These 3 positions, labeled as Positions 1, 2 and 3, are 5 m, 10 m and 15 m away from the explosive circle with a radius of 15 m, respectively (Fig. 11). As can be seen from Fig. 12, the computed acceleration curves of all the 3 positions agree with the measured data generally. As expected, the amplitude of ground motion reduces gradually with the increasing distance. For example, the amplitude of the z-acceleration at Position 1 is noticeably larger than the one at Position 3.

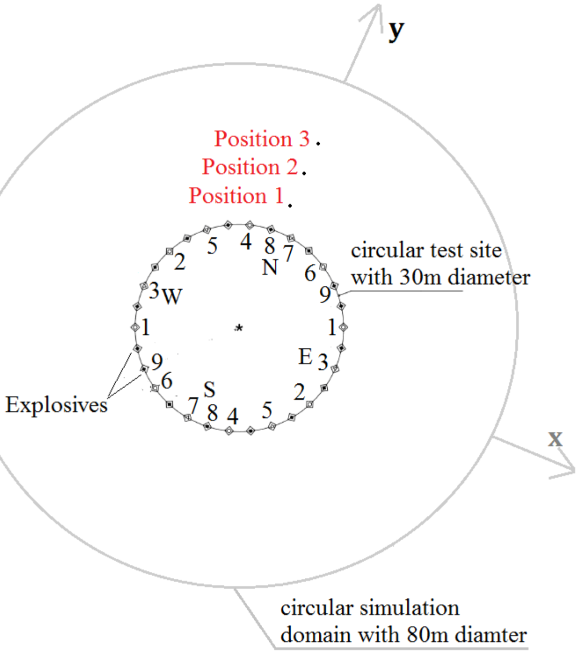

Fig. 11 Additional 3 points in the north of test site used to compare the measured and simulated vertical acceleration (UD) time histories

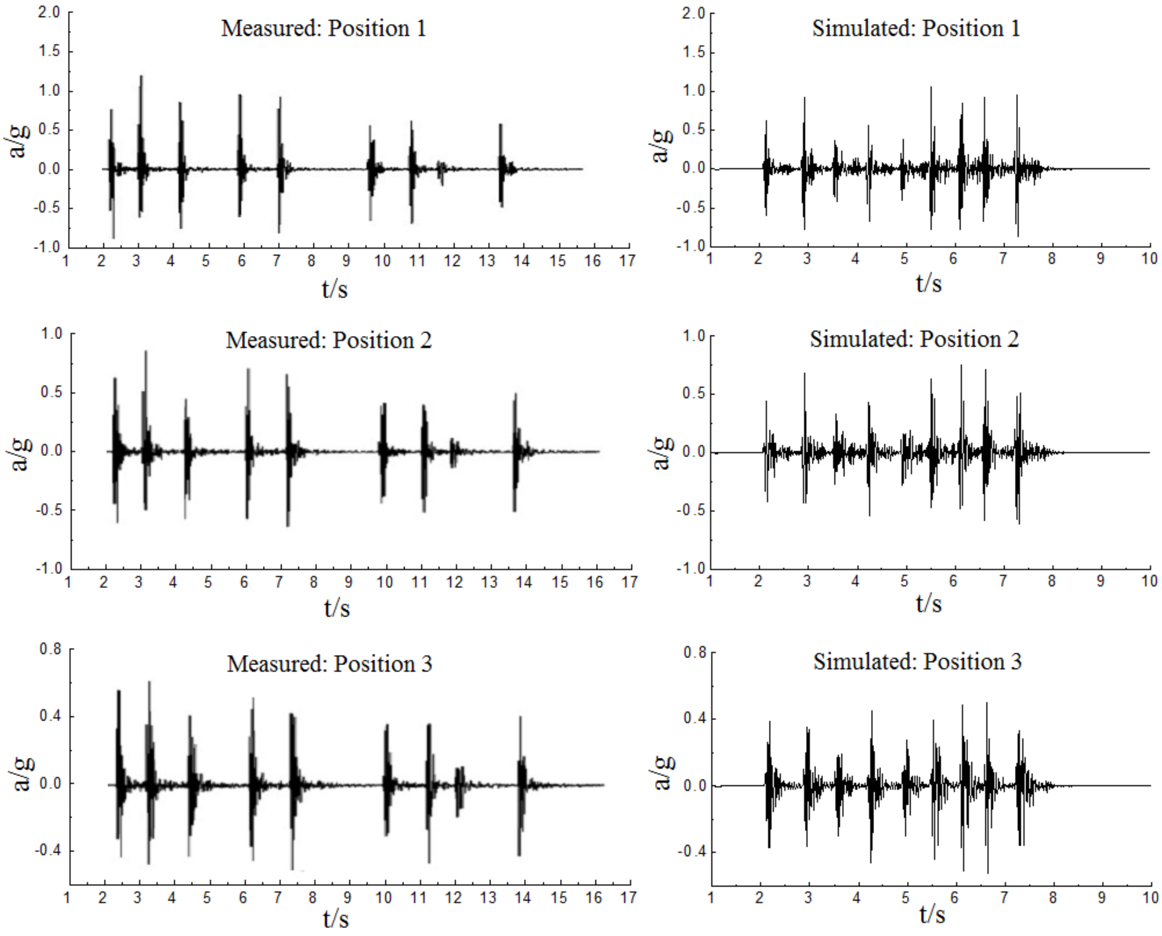

Fig. 12 Comparison of the *z*-acceleration (UD) of the 3 points in the north of test site

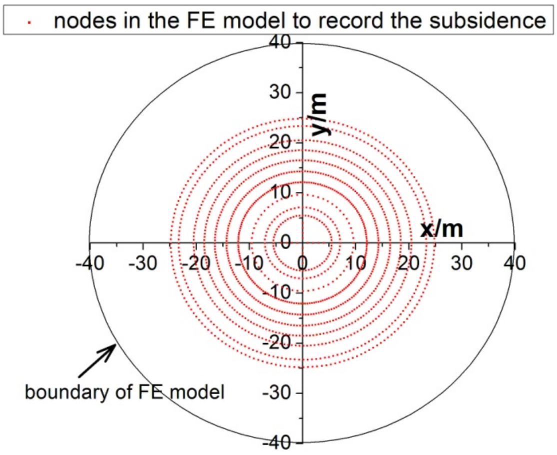

Fig. 13 Positions of nodes chosen to record the subsidence in the numerical simulation

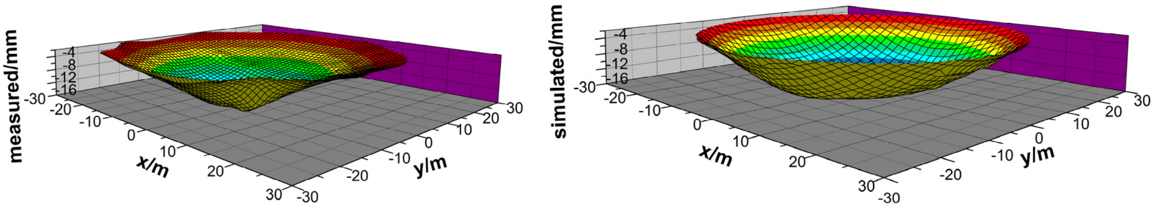

(a) Measured (b) Simulated

Fig. 14 Comparison of measured and simulated subsidence after sequential buried explosions

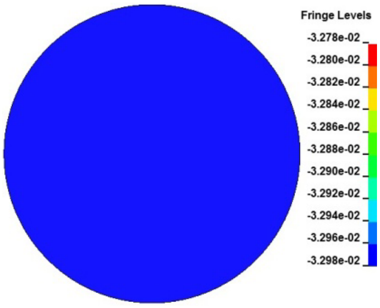

(a) After gravity

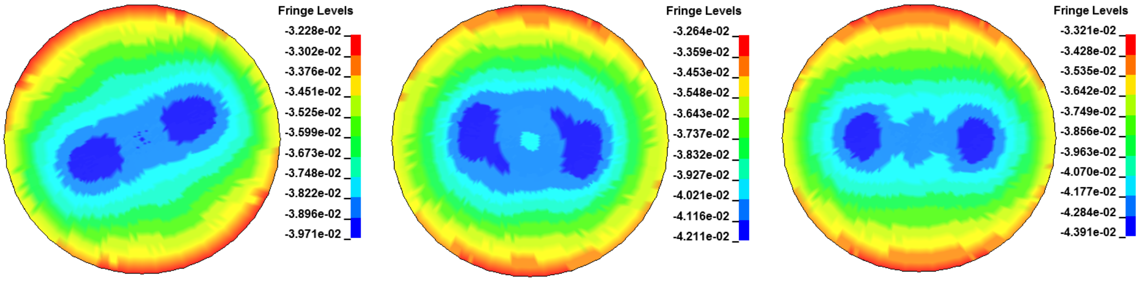

(b) After 1st blast (c) After 2nd blast (d) After 3rd blast

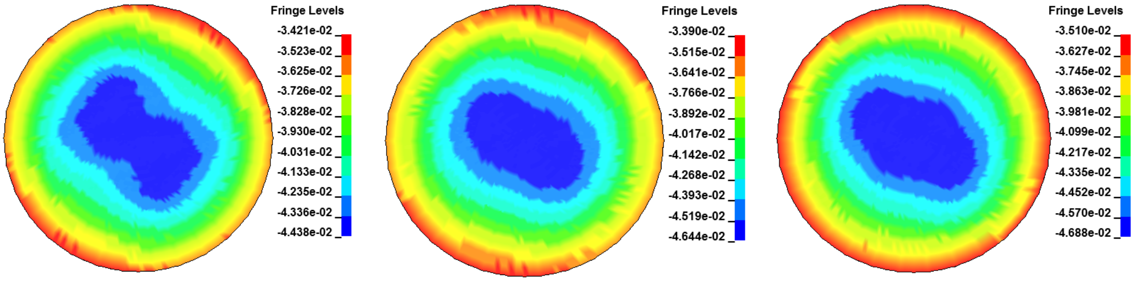

(e) After 4th blast (f) After 5th blast (g) After 6th blast

Fig. 15 Simulated accumulated vertical ground surface subsidence at each stage (Units: m)

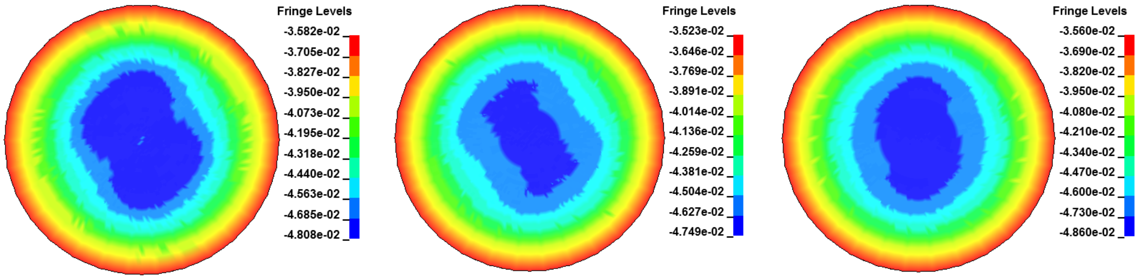

(h) After 7th blast (i) After 8th blast (j) After 9th blast

Fig. 15 Continued

4.2 Blast-induced surface subsidence

With the elastoplastic soil model employed, permanent deformation such as surface seismic subsidence was also computed by the LS-DYNA model. As an item of great engineering interest, the surface subsidence after the sequential explosion was measured at a number of stations in the field test. A comparison of the simulated and measured subsidence results at the nodes indicated in Fig. 13 after the entire sequence of detonations is given in Fig. 14 in three-dimension with a different vertical and horizontal length scale.

From Fig. 14(a), one can see that the measured data (Sun 2010) exhibits an approximate circular pattern but its lowest point is somewhat off from the center of the ring of explosive sources. With the finite element model and the material parameters chosen, the simulated subsidence shown in Fig. 14(b) is quite close to but with a somewhat smoother profile than the measured results. Given the inevitable variations of the site condition and the simplifying assumptions adopted in the numerical modeling, one can consider the deviation to be acceptable.

For further insight, the time sequence of the whole blast-subsidence process as generated by the finite element model is shown in Fig. 15. During the first detonation, for instance, the simulated subsidence is clearly localized near the two locations above the buried charges. As the detonations progress around the circle, one can see that those local depressions begin to merge (see Figs. 15(a) to (j)), eventually giving an overall profile of a shallow dish-like depression.

5. Conclusions

In this paper, a dynamic finite element modeling of a field-scale buried blast experimental test is presented. With a reasoned choice of the soil parameters for the Geological Cap model in LS-DYNA and charges as explained in the communication, the numerical results are found to compare well overall with the measured acceleration data at a level site composed of loess soils. While the computed vertical subsidence after the blast event is slightly off in profile compared to the field results, the acceleration responses at different locations are in general agreement. From the analytical simulation, for example, a better understanding of the spatial development of the soil motion from the diametrically placed sequential buried detonations is illustrated. Such knowledge gained from the finite element model should be helpful in improved planning and interpretation of blast-induced field ground motion simulation program as well as performance assessment of design of foundation and structures under similar site conditions. With the chosen soil model, engineering questions such as the possible magnitude of permanent post-earthquake ground subsidence can also be reasonably addressed. While further improvement and validation can be made with more comprehensive soil data and analytical sophistication, the beneficial use of the computational platform with the sequential field blast-induced ground motion experimental simulation approach in advancing the understanding of soil dynamics and earthquake engineering is believed to have been demonstrated.

Acknowledgments

The research described in this paper was supported by 111 Project (No. B13024), the Program for Chang Jiang Scholars and Innovative Research Team in University (No.IRT1125) and the National Natural Science Foundation of China (Grant No. 51379067).

References

Al-Qasimi, E.M.A., Charlie, W.A. and Woeller, D.J. (2005), "Canadian liquefaction experiment (CANLEX) blast-induced ground motion and pore pressure experiments", *Can. Geotech. J.*, **1**(28), 1-13.

Ashford, S., Rollins, K. and Lane, J. (2004), "Blast-induced liquefaction for full-scale foundation testing", *J. Geotech. Geoenviron. Eng.*, **130**(8), 798-806.

Ashlock, J.C., Drnevich, V.P. and Pak, R.Y.S. (2013), "Strain measures for transfer function approaches to resonant column testing", *Geotech. Test. J.*, **36**(4), 455-465.

Bates, C.R. (1989), "Dynamic soil property measurements during triaxial testing", *Geotechnique.*, **39**(4), 721-726.

Chen, W.F. and Saleeb, A.F. (1994), *Constitutive Equations for Engineering Materials: Elasticity and Modeling*, Volume 1, Elsevier, Amsterdam, Netherlands.

DiMaggio, F.L. and Sandler, I.S. (1971), "Material model for granular soils", *J. Eng. Mech. Div.*, **97**(EM3), 935-950.

Dou, H. and Byrne, P.M. (1997), "Model studies of boundary effect on dynamic soil response", *Can. Geotech. J.*, **34**(3), 460-465.

Elgamal, A., Yang, Z.H., Lai, T., Kutter, B. and Wilson, D. (2005), "Dynamic response of saturated dense sand in laminated centrifuge container", *J. Geotech. Geoenviron. Eng.*, **131**(5), 598-609.

Fung, Y.C. and Tong, P. (2001), *Classical and Computational Solid Mechanics*, World Scientific, New York, NY, USA.

Gao, X., Ling, X.Z., Tang, L. and Xu, P.J. (2011), "Soil-pile-bridge structure interaction in liquefying ground using shake table testing", *Soil Dyn. Earthq. Eng.*, **31**(7), 1009-1017.

Garga, V.K. (1988), "Effect of sample size on shear strength of basaltic residual soils", *Can. Geotech. J.*, **25**(3), 478-487.

Hallquist, J.O. (2012), *LS-DYNA Keyword User's Manual* (*971 R6.0.0*), Livermore Software Technology Corporation, Livermore, CA, USA.

Henrych, J. (1979), *The Dynamics of Explosion and its Use*, World Scientific, New York, NY, USA.

Kim, K.M. (2009), "Design of roadside barrier systems placed on mechanically stabilized earth (MSE) retaining walls", Ph.D. Dissertation, Texas A&M University, College Station, TX, USA.

Li, B.X., Niu, Y.H. and Miao, T.D. (2007), "Physico-mechanical characteristics of Malan loess in Lanzhou region", *Rock Soil Mech.*, **28**(6), 1077-1082. [In Chinese]

Liu, H.Y., Yang, J. and Chen, P.W. (2004), "Simulation of the process of explosion funnel formulation by means of discontinuous deformation analysis", *Rock Soil Mech.*, **10**(2), 17-20. [In Chinese]

Luo, Y.S. (2000), "Experimental study of dynamic properties and parameters of typical loess in china", Ph.D. Dissertation, Xi'an University of Technology, Xi'an, China.

Mamalis, A.G., Theodorakopoulos, I.D. and Vortselas, A.K. (2011), "Optimisation of the explosive compaction process for powder-in-tube MgB2 superconductors using numerical simulations", *Technische Mechanik*, **32**(4), 416-424.

Nair, A.M. and Latha, M.G. (2012), "Taming of large diameter triaxial setup", *Geomech. Eng., Int. J.*, **4** (4), 251-262.

Pak, R.Y.S., Soudkhah, M. and Abedzadeh, F. (2011), "Experimental synthesis of seismic horizontal free-field motion of soil in finite-domain simulations with absorbing boundary," *Soil. Dyn. Earthq. Eng.*, **31**(11), 1529-1539.

Rutherford, C.J. and Biscontin, G. (2013), "Development of a multidirectional simpleshear testing device", *Geotech. Test. J.*, **36**(6), 858-866.

Santagata, M. and Germaine, J.T. (2005), "Effect of OCR on sampling disturbance of cohesive soils and evaluation of laboratory reconsolidation procedures", *Can. Geotech. J.*, **42**(2), 459-474.

Sun, J.J. (2010), "Study on seismic subsidence of loess and negative skin friction along piles by field test", Ph.D. Dissertation, Lanzhou University, Lanzhou, China.

Vaid, Y.P. and Sivathayalan, S. (1996), "Static and cyclic liquefaction potential of fraser delta sand in simple shear and triaxial tests", *Can. Geotech. J.*, **33**(2), 281-289.

Wang, L.M., He, K.M., Shi, Y.C. and Wang, J. (2002), "Study on liquefaction of saturated loess by in-situexplosion test", *Earthq. Eng. Eng. Vib.*, **1**(1), 50-56.

Wang, L.M., Sun, J.J., Huang, X.F., Xu, S.H., Shi, Y.C., Qiu, R.D. and Zhang, Z.Z. (2011a), "A field testing study on negative skin friction along piles induced by seismic subsidence of loess", *Soil Dyn. Earthq. Eng.*, **31**(1), 45-58.

Wang, L.P., Zhang, G. and Zhang, J.M. (2011b), "Centrifuge model tests of geotextile-reinforced soil embankments during an earthquake", *Geotext. Geomembr.*, **29**(3), 222-232.

PL